Received: 19 April 2020 | Revised: 18 December 2020 | Accepted: 18 December 2020

DOI: 10.1002/eqe.3414

RESEARCH ARTICLE

WILEY

A new effective stress method for nonlinear site response analyses

Guoxing Chen[1,2] | **Yanzhen Wang**[1,2] | **Dingfeng Zhao**[1,2] | **Kai Zhao**[1,2] | **Jun Yang**[3]

[1] Institute of Geotechnical Engineering, Nanjing Tech University, Nanjing, China

[2] Civil Engineering and Earthquake Disaster Prevention Center of Jiangsu Province, Nanjing, China

[3] Department of Civil Engineering, The University of Hong Kong, Hong Kong, China

Correspondence
Guoxing Chen, Institute of Geotechnical Engineering, Nanjing Tech University, Nanjing 210009, China.
Civil Engineering and Earthquake Disaster Prevention Center of Jiangsu Province, Nanjing 210009, China.
Email: gxc6307@163.com

Abstract

A generic loosely coupled effective stress method is presented in this article for one-, two- and three- dimensional (1D, 2D and 3D) nonlinear site response analyses. In this method, the 1D non-Masing hysteretic constitutive model of Chen et al (2020) is extended into 2D and 3D stress conditions, by presenting a clever generalized formulation of equivalent shear strain (γ_{eq}). The element-level simulation tests show that the proposed algorithm of γ_{eq} is conceptually simple with high precision to capture the strain reversals under complex multidirectional shakings. The coupling between the cyclic stiffness degradation and the excess pore water pressure (EPWP) generation during irregular cyclic loadings is established using the proposed algorithm of γ_{eq} in conjunction with the Chen et al (2019a) EPWP generation model and the extended non-Masing hysteretic constitutive model. The simulations of the undrained cyclic triaxial tests using the new effective stress method reproduce excellently the observed response of the saturated sand specimens, demonstrating the ability to represent the undrained behavior of liquefiable sands during uniform cyclic loadings. The new effective stress method is then used to simulate the response of a downhole array liquefied site in Japan, which shows an excellent agreement between the simulations and the recordings in both horizontal and vertical components of ground motions at different depths.

KEYWORDS

earthquake liquefaction, effective stress method, equivalent shear strain algorithm, nonlinear site response

1 | INTRODUCTION

Nonlinear site response analyses require approximating the highly nonlinear stress-strain responses of soils, including the liquefaction accompanied by the drastic loss of strength in cohesionless soils and cyclic softening with significant strength loss and deformation in low-plasticity silty and clayey soils caused by the generation of excess pore water pressure.[25] Soil liquefaction or softening can modify seismic waves during strong shaking events and generate adverse influence on site response.[58,60] Therefore, seismic building codes usually require that the site response analyses be conducted to develop the site-specific design response spectra or seismic motion parameters at liquefiable sites, for example, Site Class F in the International Building Code.[24] The evaluation of liquefaction-related damage severity of buildings, buried pipelines, and infrastructures is required for the sites susceptible to liquefaction. The responses of liquefaction susceptible soil deposits with different liquefaction depth, thickness, and severity can strengthen or mitigate the liquefaction manifestations at the ground surface. Effective stress analyses are needed to illustrate the major mechanisms of liquefied soil response. An improved understanding of strong ground motion characteristics recorded at liquefied sites is also needed. Unfortunately, available strong ground motion recordings at liquefied sites are very few. While nonlinear seismic site effects have been numerically studied in the last few decades, the site response analyses of liquefied sites remain a challenging issue due to the specific requirement for advanced constitutive models.

The site response of liquefied soils due to strong earthquake events is ruled by the complex mechanical processes, which may mainly be due to the hysteresis nonlinearity (dominating strain-dependent shear modulus reduction and damping increase) and the shear-compressional coupling (dominating EPWP generation and cyclic softening). A simple and proper description of the cyclic behavior of soils includes (1) the initial loading skeleton form and (2) the unloading/reloading hysteretic behavior. Phillips and Hashash[47] presented a non-Masing hysteresis formulation for best fitting the measured shear modulus and damping of soil using the specific modulus reduction and damping factor approach. Thereafter, the Phillips and Hashash[47] formulation was effectively applied to the general quadratic/hyperbolic skeleton curves and the unloading-reloading equations of Groholski et al[11] constitutive model. Unfortunately, the application of the Phillips and Hashash[47] formulation to other skeleton functions is difficult due to the specific unloading-reloading formula involved. Note that the Phillips and Hashash[47] formulation is consistent with the Numanoglu et al[44] generalized formula applied to any skeleton function. More recently, Chen et al[6] presented a simple and creative generalized non-Masing hysteresis model, which is able to better characterize the nonlinear and hysteretic behavior of soils over a wide range of strains subjected to irregular cyclic loading sequences. The loosely coupled nonlinear effective stress analyses of soil deposits that predict the generation of EPWP by adopting semiempirical stress-based or strain-based EPWP models incorporated in hysteresis stress-strain models (eg, Refs. 19, 22, 39, and 52 among many others) are often used, and most studies focus on evaluating the capability and applicability for 1D nonlinear site responses with and without significant EPWP generation due to strong earthquake events (eg, Refs. 22, 36, 45, and 60 among many others). More advanced soil constitutive models for adequately simulating liquefaction susceptible soil behavior have been formulated within the critical state framework. The fully coupled nonlinear effective stress analyses of soil deposits, based on the coupled solid-fluid formulation that calculates both the EPWP and the stress-strain response using an advanced plasticity-based constitutive model (with no available generic material parameters) (eg, Refs. 1, 2, 12, 13, 15, 28, 35, 58, and 59 among many others), are available and relatively sophisticated. For example, the PM4SAND model[1] follows from the stress-ratio controlled and bounding surface plasticity formulation within the critical state framework, and it is limited to the in-plane stress state to simplify the formulation.

Olson et al[45] concluded that the 1D nonlinear effective stress analyses with the Vucetic and Dobry[54] EPWP generation model can correctly assess liquefaction at the free-field sites over a wide range of relative density (D_r). However, there has never been consensus on which of the EPWP generation models are more suitable for practical application. For examples, the DESRAMOD program[53] employed the strain-based EPWP generation model of Dobry et al,[17] subsequently modified by Vucetic and Dobry[54]; both the D-Mod2000[39] and the DEEPSOIL[22] programs employed the strain-based EPWP model of Matasovic and Vucetic[38]; and the SCOSSA program[10] employed the stress-based EPWP generation model of Park et al.[46] The recently proposed strain-based EPWP generation model of Chen et al[7] provided some new insights into the mechanics of the residual EPWP generation. The Chen et al[7] model and the Dobry et al[17] model are significantly different in mechanism of the EPWP generation. The Dobry et al[17] model and the Chen et al[7] model follow from, respectively, the constant and the nonconstant volumetric strain incremental tendency per cycle at a constant cyclic shear strain amplitude. The Chen et al[7] model and the Martin et al[37] model, subsequently modified by Byrne,[3] differ by a key assumption. In the Chen et al[7] model, the EPWP generation is quantified by the volumetric strain changes, their correlation equation is linked with bulk modulus. The Chen et al[7] model equation simplified the Martin et al[37] model for determining the elastic rebound modulus, and also offers an improvement over the Byrne[3] model equation by incorporating a clear physics-based threshold shear strain. In addition, the stress-based Seed et al[50] model and the strain-based Dobry et al[17] model, widely used, and their modified versions, are functions of the number of uniform cycles for the scenario earthquake in evaluating the EPWP generation. This implies that it is necessary to convert an irregular earthquake motion to the equivalent uniform shear stress or strain cycles, but there is no consensus on the number of equivalent uniform cycles for assessing liquefaction triggering. The assumption that the equivalency of stress cycles is the same as the equivalency of strain cycles is uncertain.[43] However, the Chen et al[7] model equation is independent of the number of loading cycles, can bypass such conversion procedure, and is applicable to irregular stress or strain cycles. Dobry and Abdoun[16] reiterated that cyclic shear strain plays a determinative role in saturated sand liquefaction. Therefore, it is desirable to predict the EPWP generation from the strain response in saturated sandy deposits subjected to strong earthquake shaking.

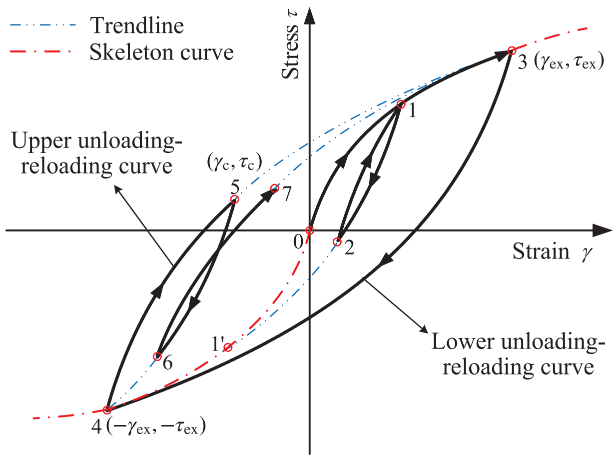

FIGURE 1 Shear stress-strain curves of irregular loading-unloading-reloading

This article focuses on the development of a generic loosely coupled effective stress method for nonlinear site response analyses of liquefaction sites. Given the advantages of the 1D generalized non-Masing hysteretic constitutive model of Chen et al,[6] this article first extends the 1D non-Masing hysteretic model to the 2D and/or 3D stress conditions. Furthermore, considering the merits of the Chen et al[7] EPWP generation model in physical mechanism, a loosely coupled effective stress method is then developed in ABAQUS/Explicit platform,[18] and the Chen et al[7] EPWP generation model is integrated into the expanded generalized non-Masing hysteretic constitutive model to describe the sophisticated behavior of liquefaction susceptible soils due to strong shaking events. Finally, the proposed effective stress method is verified through the 3D simulation of undrained cyclic triaxial tests as well as the seismic responses of the downhole seismic array site in Japan.

2 | NONLINEAR CONSTITUTIVE MODEL OF SOIL

2.1 | Generalized non-Masing hysteretic model of Chen et al[6]

A set of non-Masing rules for irregular cyclic loading sequences associated with earthquakes are used to model the 1D nonlinear and hysteretic stress-strain behavior of soil (see Figure 1). The simple and creative 1D generalized non-Masing hysteretic constitutive model based on the Davidenkov skeleton curve (hereafter termed the Davidenkov-Chen- Zhao model, ie, DCZ model) is stated as follows[6]:

(1) For the initial loading, the shear stress-strain skeleton curve is expressed as

$$\tau = F_{sk}(\gamma) = G_{\max}\gamma\left[1 - H(\gamma)\right], \tag{1}$$

where τ is shear stress; $G_{\max}$ is initial shear modulus; $F_{sk}(\gamma)$ is generalized hyperbolic skeleton curve as the function of shear strain (γ), $H(\gamma)$ is the function describing the shape of stress-strain relationship, expressed in the Davidenkov form

$$H(\gamma) = \left\{\frac{(\gamma/\gamma_r)^{2B}}{1 + (\gamma/\gamma_r)^{2B}}\right\}^{A}, \tag{2}$$

where A and B are the nondimensional constants for adjusting the shape of the skeleton curve to allow more flexibility in characterizing nonlinear behavior of soils; γ_r is the reference shear strain for the soil in question.

(2) If the strain reverses, the subsequent shear stress-strain path follows subsequently the curve with Equation (3) from the current strain reversal point to the last strain extreme point in the previous irregular loading cycles

$$\tau - \tau_c = G_{\max}(\gamma - \gamma_c)\left[1 - H\left(\frac{|\gamma - \gamma_c|}{2n_c}\right)\right] \tag{3}$$

in which

$$(2n_c\gamma_r)^{2B} = (\gamma_{ex} \pm \gamma_c)^{2B} \cdot \left(\frac{1-R}{R}\right), \tag{4}$$

$$R = \left(1 - \frac{\tau_{ex} \pm \tau_c}{G_{\max}(\gamma_{ex} \pm \gamma_c)}\right)^{\frac{1}{A}}, \tag{5}$$

where n_c is the scaling factor controlling the size of hysteresis loops; the sign "±" is negative for the upper unloading-reloading curve and positive for the lower unloading-reloading curve during the irregular cyclic loading sequences, respectively (see Figure 1); τ_c and γ_c is the shear stress and strain at the current strain reversal point, respectively; τ_{ex} and γ_{ex} is the shear stress and strain at the last strain extreme point, respectively.

(3) If the unloading/reloading shear stress-strain path overlaps the skeleton curve, it moves along the skeleton curve to the next shear strain reversal.

To capture the influence of soil depth on the normalized shear modulus ($G/G_{\max}$) and damping ratio (ξ) curves, a formulation is introduced in which the γ_r is an effective overburden pressure-dependent variable as follows[21]:

$$\gamma_r = a_1\left(\sigma'_{v0}/\sigma'_{ref}\right)^{a_2}, \tag{6}$$

where a_1 and a_2 are dimensionless constants for the soil in question; σ'_{v0} is the initial effective overburden pressure at the depth in question; σ'_{ref} is a reference overburden pressure of 180 kPa.

As shown in Figure 1, under the irregular loading-unloading-reloading sequences, when a strain reversal occurs, the current reversal point defined by the coordinates (τ_c, γ_c) needs to be remembered for determining the subsequent path orientation of shear stress-strain curve; the desired stress-strain paths follow a consecutive path along curve 0→1→2→3→4→5→6→7. Therefore, the Equations (1) and (3) represent a hyperbolic type of skeleton curve and non-Masing hysteretic behavior of soil, respectively; the set of non-Masing criteria (1) to (3) has the merits of simpleness and exactness in capturing the strain reversal points, and can determine the subsequent stress-strain paths with no need for keeping track of the previous stress-strain paths. In addition, the scaling factor n_c is updated at each irregular cycle to match simultaneously the measured shear modulus and damping in a wide range of strains. The $n_c = 1.0$ for the strain reversal points at the skeleton curve, whereas the $n_c < 1.0$ for the strain reversal points at the subsequent irregular stress-strain loops of partial cycles. Specifically, cyclic softening (shear modulus degradation) of soil can be simulated by applying the $n_c < 1.0$.

The tangential shear modulus G^t for the initial skeleton curve Equation (1) is expressed as

$$G^t = \frac{\partial \tau}{\partial \gamma} = G_{\max}\left[1 - \left(1 + \frac{2AB{\gamma_r}^{2B}}{{\gamma_r}^{2B} + \gamma^{2B}}\right) \cdot H(\gamma)\right]. \tag{7}$$

The G^t for the unloading-reloading curve Equation (3) is expressed as

$$G^t = \frac{\partial(\tau - \tau_c)}{\partial(\gamma - \gamma_c)} = G_{\max}\left\{1 - \left[1 + \frac{2AB(2n_c\gamma_r)^{2B}}{(2n_c\gamma_r)^{2B} + |\gamma - \gamma_c|^{2B}}\right] H\left(\frac{|\gamma - \gamma_c|}{2n_c}\right)\right\}, \tag{8}$$

where the superscript t refers to the start of an incremental time in explicit dynamic analysis.

2.2 | Generalized formulation of the equivalent shear strain

When the 1D shear stress-strain relationship which followed the DCZ model is extended to either 2D or 3D stress conditions, the form of the shear stress-strain relationship remains unchanged, with the equivalent stress-strain relationship being used to replace that in the 1D shear stress-strain relationship, thus yielding the results that are consistent with the experimental data of the $G/G_{\max}$ and ξ curves. The octahedral or generalized shear strain in 2D or 3D stress conditions is commonly used as the equivalent shear strain (γ_{eq}) instead of shear strain.[6,23] The DCZ model using the generalized shear

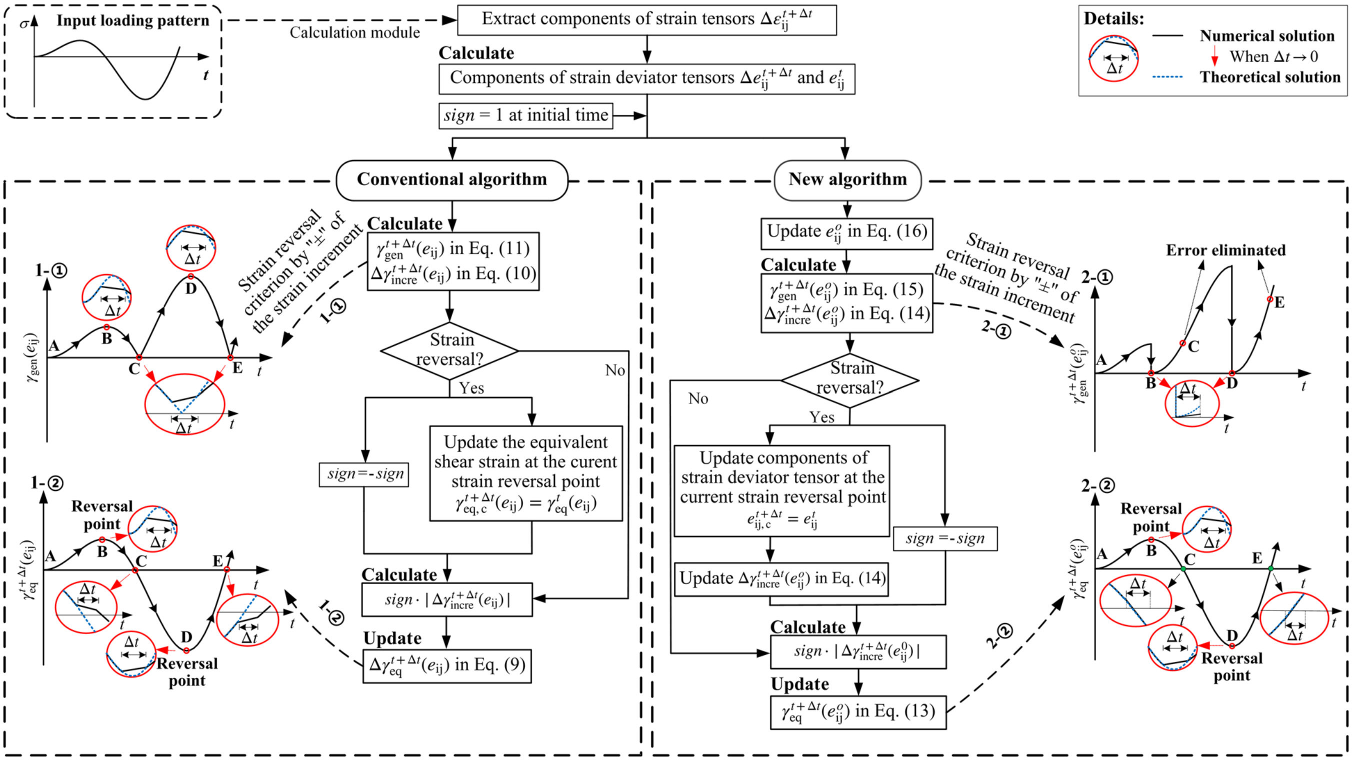

FIGURE 2 Comparison of the difference between the new and conventional equivalent shear strain algorithms in the implementation processes

strain as the γ_{eq} has been tested in 2D and 3D nonlinear seismic response analyses of large-scale seabed site, submarine tunnel, underground structure, and nuclear island structure on soft rock during the three years.[6,31,40,41,49]

As shown in Figure 2 (left), the incremental form of the conventional algorithm of γ_{eq} can be described as follows

$$\gamma_{eq}^{t+\Delta t}\left(e_{ij}\right) = \gamma_{eq}^{t}\left(e_{ij}\right) + sign \cdot \left|\Delta\gamma_{incre}^{t+\Delta t}\left(e_{ij}\right)\right| \tag{9}$$

in which

$$\Delta\gamma_{incre}^{t+\Delta t}\left(e_{ij}\right) = \gamma_{gen}^{t+\Delta t}\left(e_{ij}\right) - \gamma_{gen}^{t}\left(e_{ij}\right), \tag{10}$$

$$\gamma_{gen}^{t+\Delta t}\left(e_{ij}\right) = \sqrt{4J_2^{t+\Delta t}\left(e_{ij}\right)/3}, \tag{11}$$

where "*sign*" = 1 for the upper unloading-reloading curve and "*sign*" = −1 for the lower unloading- reloading curve during unloading/reloading (see Figure 1), respectively; the superscripts t and $t + \Delta t$ refers to the start and end of time steps in an explicit dynamic analysis, respectively; Δt is time step size; e_{ij} is deviatoric strain tensor taking γ as an independent variable, $\gamma_{gen}(e_{ij})$ is the generalized shear strain of e_{ij}, $J_2(e_{ij})$ is the second invariants of the e_{ij}.

To determine the orientation of the subsequent irregular cyclic loading paths, the curve 1-① in Figure 2 (left) should be converted to the equivalent shear strain curve 1-② with consistent strain path. For this purpose, the vector $\vec{\varepsilon}$ is defined as follows

$$\vec{\varepsilon} = \left\{\varepsilon_{11} - \varepsilon_m, \varepsilon_{22} - \varepsilon_m, \varepsilon_{33} - \varepsilon_m, \sqrt{2}\varepsilon_{11}, \sqrt{2}\varepsilon_{12}, \sqrt{2}\varepsilon_{23}\right\}, \tag{12}$$

where ε_{ij} is the strain tensor, ε_m is the volumetric strain.

If $\Delta\gamma_{incre}^{t+\Delta t}(e_{ij}) < 0$ and $\Delta\gamma_{incre}^{t+\Delta t}(e_{ij}) \cdot \Delta\gamma_{incre}^{t}(e_{ij}) < 0$, or if $\Delta\gamma_{incre}^{t+\Delta t}(e_{ij}) \cdot \Delta\gamma_{incre}^{t}(e_{ij}) < 0$ and the dot product $\Delta\vec{\varepsilon}^{t} : \Delta\vec{\varepsilon}^{t+\Delta t} < 0$ (where $\Delta\vec{\varepsilon} = \vec{\varepsilon}^{t+\Delta t} - \vec{\varepsilon}^{t}$), a shear strain reversal is expected to occur. If the value of $\Delta\gamma_{incre}^{t+\Delta t}(e_{ij})$ at the "sign" changing point is smaller than its actual value, a calculation error occurs. As shown in the curve 1-① plotted in Figure 2 (left), two kinds of errors occur in the conventional algorithm of γ_{eq}. One occurs at the actual strain reversal points B and D

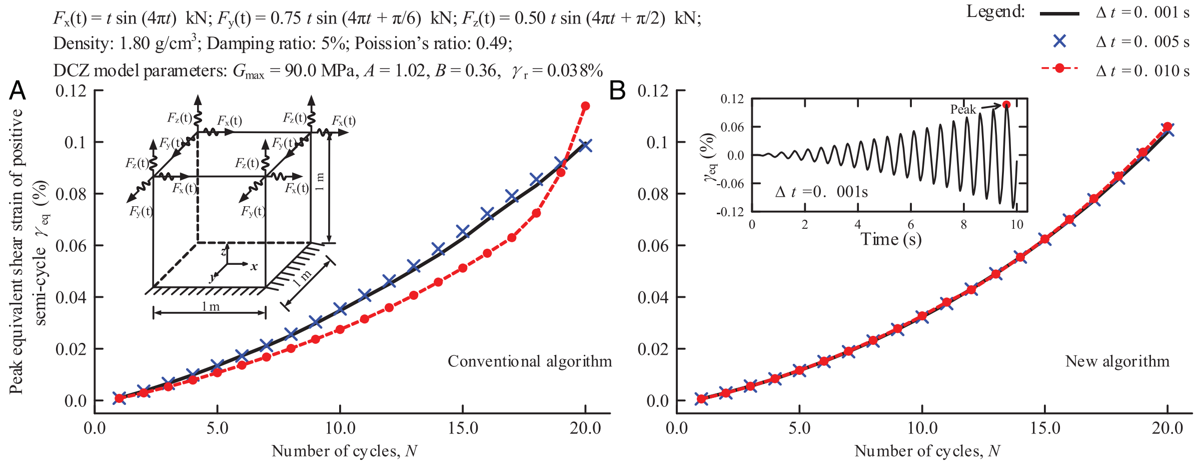

FIGURE 3 Influence of time step sizes Δt on the amplitudes and precisions of equivalent shear strain (γ_{eq}) simulated by the new and conventional algorithms under tridirectional shakings

in Figure 2 (left), the corresponding error is the difference between the theoretical and numerical shear strain reversal points. The other one occurs at the false strain reversal points C and E in Figure 2 (left), the corresponding error is caused by the failure to capture the point $\gamma_{gen}^{t+\Delta t}(e_{ij}) = 0$.

The errors at the false strain reversal points can be eliminated in a clever algorithm. Because of the renewal of the shear stress in Equation (3) involves the shear strain bias $(\gamma - \gamma_c)$, a new deviatoric strain tensor e_{ij}^o is defined by using $(\gamma - \gamma_c)$ to replace γ as an independent variable, the incremental form of the new algorithm of γ_{eq} is written as

$$\gamma_{eq}^{t+\Delta t}\left(e_{ij}^o\right) = \gamma_{eq}^t\left(e_{ij}^o\right) + sign \cdot \left|\Delta\gamma_{incre}^{t+\Delta t}\left(e_{ij}^o\right)\right| \tag{13}$$

in which

$$\Delta\gamma_{incre}^{t+\Delta t}\left(e_{ij}^o\right) = \gamma_{gen}^{t+\Delta t}\left(e_{ij}^o\right) - \gamma_{gen}^t\left(e_{ij}^o\right), \tag{14}$$

$$\gamma_{gen}^{t+\Delta t}\left(e_{ij}^o\right) = \sqrt{4J_2^{t+\Delta t}\left(e_{ij}^o\right)/3}, \tag{15}$$

$$e_{ij}^o = e_{ij} - e_{ij,c}, \tag{16}$$

where $J_2(e_{ij}^o)$ is the second invariant of the e_{ij}^o; $\gamma_{gen}(e_{ij}^o)$ is the generalized shear strain of the e_{ij}^o; $e_{ij,c}$ is deviatoric strain tensor at the current strain reversal point.

As shown in Figure 2 (right), in the new algorithm of γ_{eq}, a shear strain reversal will occur when $\Delta\gamma_{incre}^{t+\Delta t}(e_{ij}^o) < 0$. This shear strain reversal criterion is conceptually simple, and makes the new algorithm of γ_{eq} more precise than the conventional algorithm of γ_{eq}. The most obvious difference between the new and conventional algorithms is the path of the γ_{eq} curve (see curve 1-① vs curve 2-① in Figure 2). Note the continued growth of $\gamma_{gen}^{t+\Delta t}(e_{ij}^0)$ in the new algorithm before changes in the hysteresis path, at which point $\gamma_{gen}^{t+\Delta t}(e_{ij}^o)$ again increases from zero. That is, only the actual strain reversal points B and D in Figure 2 (right) are the "sign" changing points in the $\gamma_{gen}^{t+\Delta t}(e_{ij}^0)$ curve, whereas the calculation errors at the false strain reversal points caused by the conventional algorithm of γ_{eq} are eliminated in the new algorithm of γ_{eq}.

Figure 3 compares the conventional algorithm with the new algorithm of γ_{eq} for the element-level simulation model tests: a cubic hexahedron of size 1 m fixed at the bottom subjected to tri-directional shakings at the top four corners. The Δt of the nonlinear dynamic simulations is 0.01, 0.005, and 0.001 seconds, respectively. Figure 3 shows the simulating results using the new and conventional algorithms of γ_{eq}. The results indicate the new algorithm of γ_{eq} allows larger time step that may result in fewer incremental steps and faster solution, which greatly improves the computational efficiency for nonlinear seismic response analyses of 2D and 3D large-scale sites. Therefore, the new algorithm of γ_{eq} is robust and has higher precision than the conventional algorithm of γ_{eq}.

3 | COUPLED MODEL OF MODULUS DEGRADATION-EXCESS PORE WATER PRESSURE GENERATION

Since the pore water drainage of saturated soil is assumed not to occur during an earthquake, the slip of soil grains within the soil skeleton will cause both plastic shear and plastic volumetric strains. Chen et al[7] proposed a shear-volume strain coupling model to predict the generation of the residual EPWP (u_e) during the liquefaction of saturated sands. In the Chen et al[7] EPWP generation model, the incremental shear-volume strain coupling equation and the correlation equation between the generation of u_e during undrained cyclic triaxial (CTX) test and the accumulated volume strain (ε_{vd}) during drained CTX counterpart test are expressed as the incremental equation between Δu_e (undrained) and $\Delta\varepsilon_{vd}$ (drained) linked with the bulk modulus K

$$\Delta\, u_e = K\Delta\, \varepsilon_{vd}, \tag{17}$$

the incremental shear-volume strain coupling equation

$$\frac{\Delta\, \varepsilon_{vd}}{(\gamma_a - \gamma_{th})^{C_3}} = C_1 \exp\left(-C_2 \frac{\varepsilon_{vd}}{(\gamma_a - \gamma_{th})^{C_3}} \right), \tag{18}$$

and the correlation equation between r_u (undrained) and ε_{vd} (drained)

$$r_u = m \ln\left(n\varepsilon_{vd} + 1\right), \tag{19}$$

where C_1, C_2, C_3, m, and n are the material-specific constants, Δu_e is the EPWP value caused by one cycle of cyclic shear strain amplitude (γ_a) during an undrained CTX test, and $\Delta\varepsilon_{vd}$ is the change in volumetric strain caused by the cyclic shearing with the same cycle of γ_a during a drained CTX test. The threshold shear strain γ_{th} is defined as the γ_a below which there is no buildup of EPWP in the saturated sand specimen during the undrained CTX test. The excess pore water pressure ratio r_u is defined as the u_e normalized by initial effective consolidation stress during the undrained CTX test. The ε_{vd}, $\Delta\varepsilon_{vd}$, γ_a, and γ_{th} are in percent, and the K and Δu_e are in kilopascals. The procedures for the determination of the six constants γ_{th}, C_1, C_2, C_3, m, and n for the EPWP model have been summarized in detail by Chen et al.[7]

Differentiating r_u with respect to ε_{vd}, the bulk modulus K is obtained:

$$K = \frac{dr_u}{d\varepsilon_{vd}}. \tag{20}$$

Note that the generation of EPWP during an earthquake causes the degradation of soil shear stiffness (modulus). In terms of the concepts of cyclic stiffness degradation,[38] the preceding stress-strain skeleton curve for capturing the drained soil skeleton behavior is used to predict the undrained stress-strain skeleton curve of soil, which considers the volumetric constraint imposed by the pore water. For the loose-coupled effective stress method presented here, the cyclic stiffness degradation of a liquefied soil is represented through the modification of the above generalized non-Masing hysteresis constitutive model in which the DCZ model incorporates with the new algorithm of γ_{eq} (hereafter termed the expanded DCZ model), that is, replacing the $G_{\max}$ and γ_r with the updating variables $G^t_{\max}$ and γ^t_r in Equations (21) and (22) by employing the r_u as the degradation index:

$$G^t_{\max} = G_{\max}\sqrt{1 - r_u}, \tag{21}$$

$$\gamma^t_r = \gamma_r\sqrt{1 - r_u} \quad \Leftrightarrow \quad \gamma^t_r = a_1\left(\sigma'_{v0}/\sigma'_{ref}\right)^{a_2}\sqrt{1 - r_u}. \tag{22}$$

Thus, the coupled model in which the expanded DCZ model is integrated with the Chen et al[7] EPWP model is a new constitutive model for the effective stress-strain behaviour of saturated soils. Consequently, this coupled model allows for the changes in shear modulus of soils due to the EPWP generation.

Note that the generation of u_e is computed at the end of each half-cycle loading and the state variables are updated at every half-cycle when the next strain reversal occurs in the stress-strain paths for irregular cyclic loading sequences.

4 NUMERICAL SCHEME

One disadvantage of commercial software is that they fail to provide all the materials that the users desire. Such difficulty can be overcome by the addition of user programmable subroutines. To this end, based on the explicit algorithm method and parallel computing technology in ABAQUS/Explicit platform,[4,5] a user-defined material subroutine VUMAT for the DCZ model combined with the conventional algorithm of γ_{eq}, which is used in the total stress method for nonlinear site response analyses, has been successfully developed by Chen et al[6] to define the state of the material at the Gauss points within each element, and written in Fortran language. The VUMAT subroutine has been tested to conduct the 2D and 3D nonlinear seismic response analyses in a series of studies.[31,40,41,49] The proposed loose-coupled effective stress method for nonlinear site response analyses in this article is also implemented in ABAQUS/Explicit platform. To implement the proposed theory in the form of a stress update algorithm, a user-defined material subroutine VUMAT for the above coupled model, in which coupling between the expanded DCZ model and the Chen et al[7] EPWP generation model is implemented, is developed to define the state of the material at the Gauss points within each element, written in Fortran language.

The simulation of u_e generation adopts an elaborate scheme, which requires the use of continuous analysis technology to couple calculation with both static and dynamic analysis steps. The static step is used to calculate in situ geostatic stress balance for the force of gravity and the hydrostatic pressure to obtain the initial effective consolidation stress of the computational domain. The calculation of this step should use a user-defined material subroutine UMAT. To enable the initial effective consolidation stress to be invoked in the subsequent dynamic step, the state variable numbers of initial effective consolidation stress in the subroutine UMAT should be the same as the subroutine VUMAT.

In ABAQUS/Explicit method using the central-difference operator, the displacement equilibrium solution at the end of each time step is computed using the conditions of equilibrium at the beginning of each time step. The solution of the motion equation for a dynamic system is expressed as:

$$\ddot{\boldsymbol{u}}^{(i)} = \boldsymbol{M}^{-1}\left(\boldsymbol{F}^{(i)} - \boldsymbol{I}^{(i)}\right), \tag{23}$$

where $\ddot{u}$ is the acceleration vector; **M** is the lumped mass matrix, **F** is the applied load vector, and **I** is the vector of internal force, the superscript i refers to the ith incremental step in an explicit dynamic analysis. To achieve convergence for the solution in the high nonlinearity of site response analyses, the time step size Δt usually does not exceed 10^{-5} seconds in an explicit dynamic analysis. The results of the 2D and 3D nonlinear seismic response analysis[4, 5, 6, 31,49] have shown the availability and versatility of the above parallel computational method performed in ABAQUS/Explicit platform.

For anyone of Masing or non-Masing hysteretic models to describe the hysteresis stress-strain behavior of soil, nearly zero damping is encountered at very small strains. However, soil exhibits damping at very small strains. The small-strain damping (ξ_0) may be related to the effective overburden pressure, the cyclic loading pattern, the parent rock type of soil, and the soil spatial heterogeneity resulting in wave scattering.[8,19,21,51] The identified ξ_0 value from earthquake motions at downhole array sites to match the array site responses is that the laboratory-measured ξ_0 value be increased by a factor from 1.5 to 5.5.[51] Thus, for simplicity, we incorporate a constant ξ_0 or an effective overburden pressure-dependent ξ_0[21] in the ABAQUS/Explicit to resolve the nearly zero damping problem in this article.

$$\xi_0 = a_3/\left(\sigma'_{v0}\right)^{a_4}, \tag{24}$$

where a_3 and a_4 are dimensionless constants for the soil in question.

Only a portion of the site most influenced by ground motion is mapped onto the computational domain, with the remainder captured by an artificial boundary condition,[29,32,33,55] allowing the scattering waves to propagate through the cutoff boundaries toward the far-field sites without reflection. The viscous-spring artificial boundary of Liu and his colleagues,[32, 33] by transforming the bedrock input motion into the equivalent nodal loads derived by distributing the spring and dashpot system on the artificial boundary, has been proven to be effective from the results of 2D and 3D nonlinear seismic response analyses.[5,34] In the artificial boundary of Liu and his colleagues,[32, 33] uniform stress distribution in the half-interval around the artificial boundary node is assumed (see Figure 4). Given the uneven nature of this actual stress distribution, an improved method of seismic input with higher precision[61] is utilized in the article:

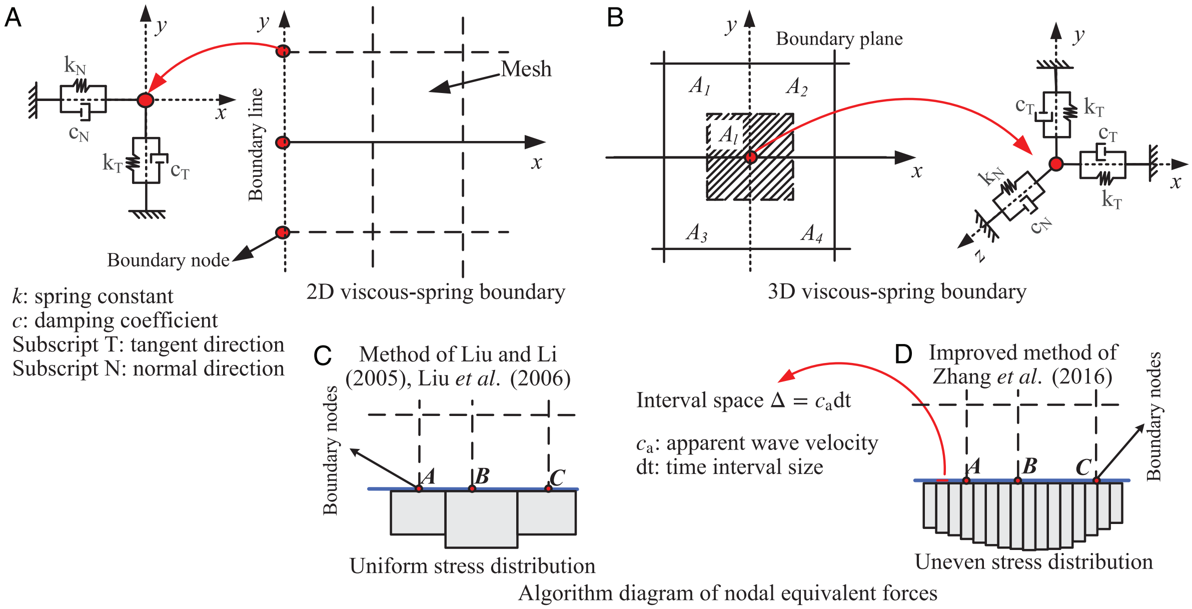

FIGURE 4 Seismic input method at the viscous-spring artificial boundary

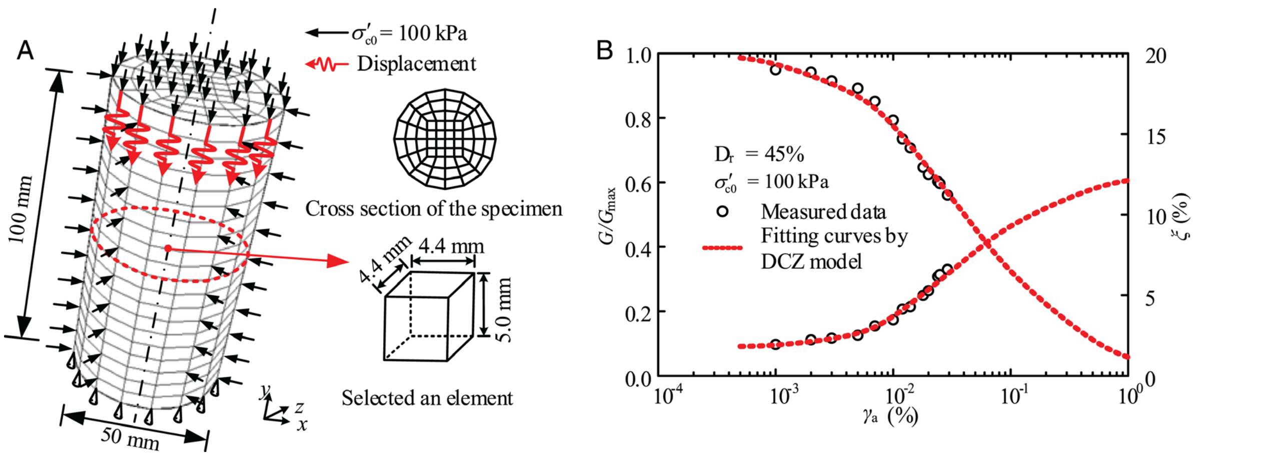

FIGURE 5 3D model and material properties for element test: (A) undrained strain-controlled cyclic triaxial test specimen; and (B) G/G_{max} versus γ_a and ξ versus γ_a curves of saturated fine sand form resonant column test

the equivalent nodal loads obtained from a mesh refinement process that combines the uneven stress integration of the half-interval around the artificial boundary node (see Figure 4). The results of 2D and 3D nonlinear seismic response analysis on seabed site and undersea shield tunnel[6,49] have shown the versatility of the improved method of seismic input.

5 | MODEL VALIDATION

5.1 | Element test

The simulation of the physical modeling tests at the element level is conducted to calibrate and validate the proposed theory in the form of the above coupled model of modulus degradation-excess pore water pressure generation. The benchmarking data for test validation are taken from the original data of the undrained strain-controlled cyclic triaxial tests and the resonant column test of Chen et al[7] for the saturated fine sand with relative densities D_r = 35%-60%. The cyclic undrained responses of the specimens representing by the 3D cylindrical model are simulated using the proposed effective stress method. As shown in Figure 5(A), the soil specimen is discretized into 1280 elements. The vertical freedom at the bottom of the specimen is fixed; the displacement D_{dis} $(t) = -0.1\varepsilon_a \sin(2\pi t)$ m is applied on the top surface of

TABLE 1 Parameters for the simulation of the undrained cyclic triaxial testes for saturated fine sand

			DCZ model					Excess pore water pressure model					
Relative density D_r (%)	**Density ρ (g/cm^3)**	**Dynamic Poisson ratio**	**G_{max} (MPa)**	**A**	**B**	**γ_r (%)**	**a_3**	**C_1**	**C_2**	**C_3**	**γ_{th} (%)**	**m**	**n**
35	1.81	0.49	48	1.02	0.43	0.041	0.45	1.164	0.129	1.25	0.02	0.345	6.689
45	1.83		53					1.051	0.143				
50	1.84		54					0.997	0.150				

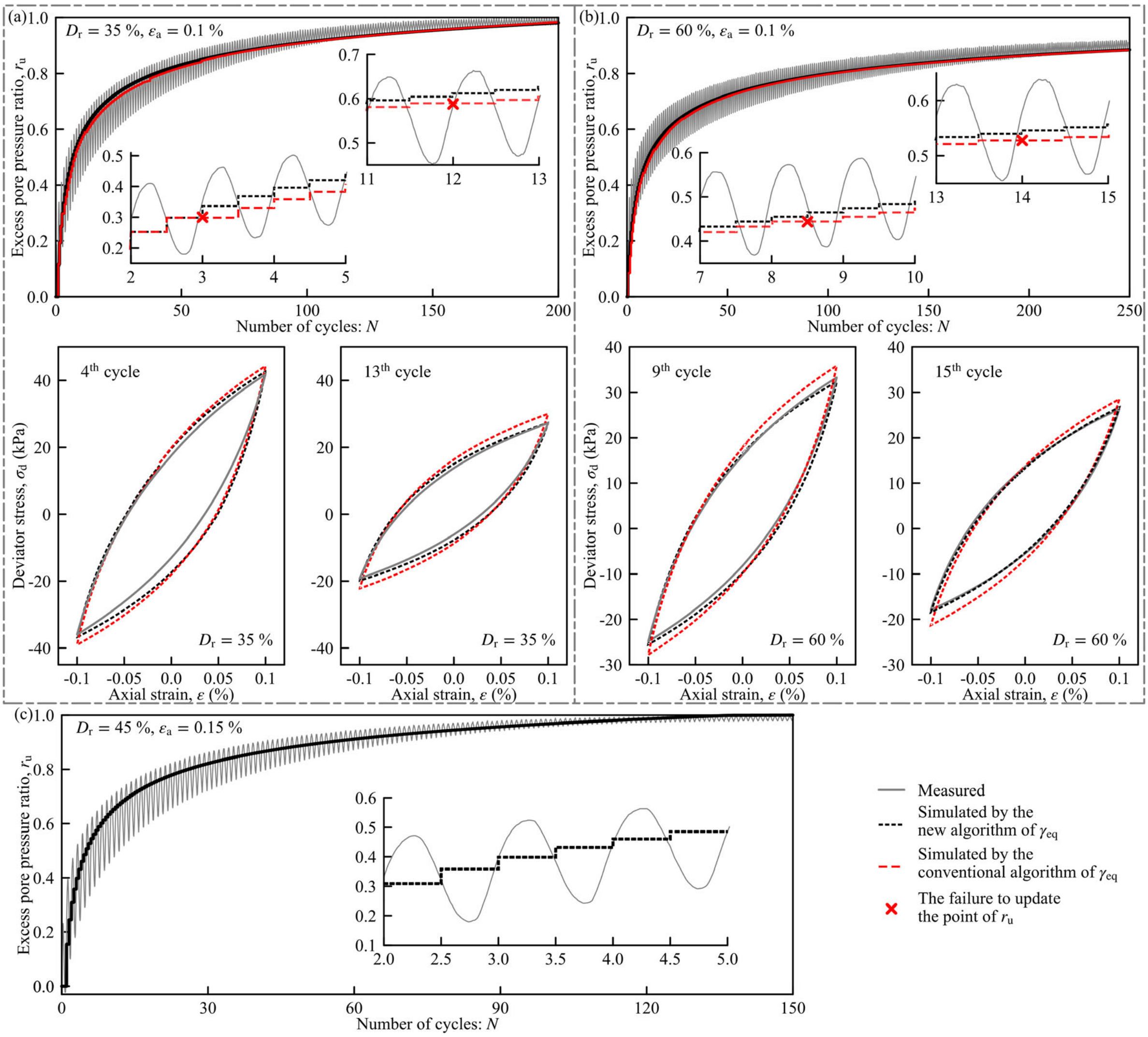

FIGURE 6 Comparison of the simulated and measured time-histories of r_u for different relative densities (D_r) and axial strain amplitudes (ε_a) in undrained strain-controlled cyclic triaxial tests. In the explicit dynamic analysis, time step $\Delta t = 1 \times 10^{-4}$ seconds

the specimen, where ε_a is the amplitude of cyclic axial strain applied. The variation of G/G_{max} and ξ with shear strain amplitude γ_a for the sand specimen with $D_r = 45\%$ are shown in Figure 5(B), and the corresponding parameters of the DCZ model are given in Table 1. The parameters of the Chen et al[7] EPWP model are also given in Table 1.

Figure 6 compares the measured data with the simulated time-histories of excess pore water pressure ratio r_u by the proposed loose-coupled effective stress method. In Figure 6, the simulated generations of r_u by the proposed effective stress method agree well with the measured data from the three validation tests, which clearly indicate a stair-like update of the simulated r_u at each half-cycle. In addition, Figures 6(A) and 6(B) exemplify the conventional algorithm of γ_{eq} failed

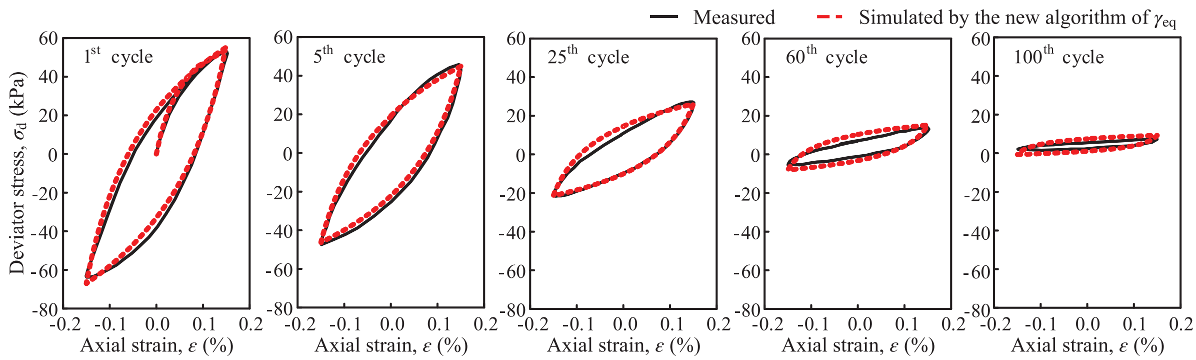

FIGURE 7 Comparison of the simulated and measured axial stress-strain relationships for the relative density $D_r = 45\%$ and the applied cyclic axial strain amplitude $\varepsilon_a = 0.15\%$. In the explicit dynamic analysis, time step: $\Delta t = 1 \times 10^{-4}$ seconds

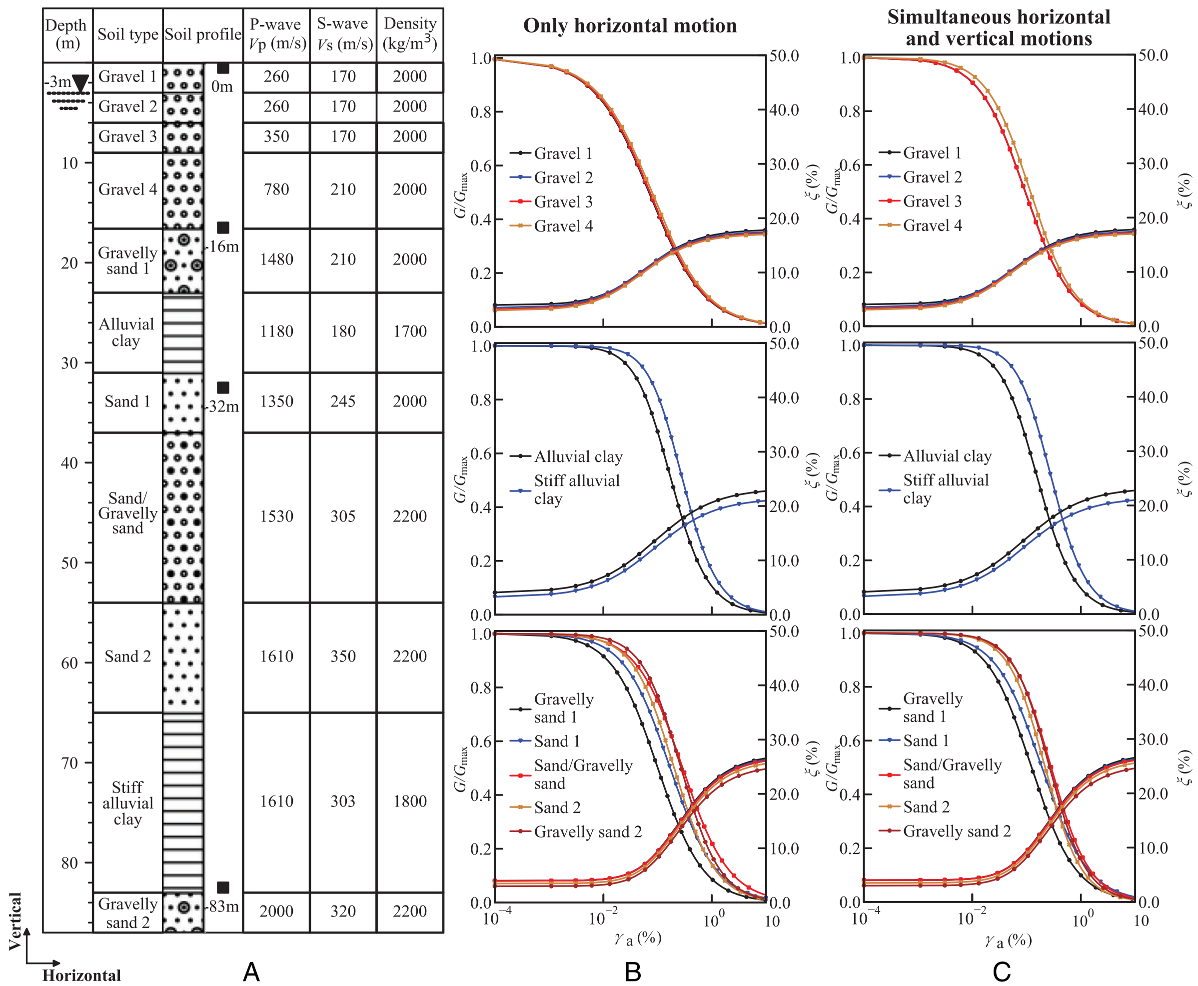

FIGURE 8 Port Island borehole array site and cyclic behavior of soils: (A) the soil profile, the S- and P-wave velocity profiles, soil densities, and the depths of strong motion seismographs; (B) G/G_{max} versus γ_a and ξ versus γ_a curves of soils for unidirectional (horizontal) shaking; and (C) G/G_{max} versus γ_a and ξ versus γ_a curves of soils curves for bidirectional (horizontal and vertical) shaking

to a stair-like update of the generations of r_u at some cycles of cyclic loadings, for example, at the 3th and 12th cycles in Figure 6(A) and at the 8.5th and 14th cycles in Figure 6(B). Consequently, compared with the conventional algorithm of γ_{eq}, the simulated hysteresis loops corresponding to the 4th and 9th cycles in Figure 6(A) and the 9th and 15th cycles in Figure 6(B) by the new algorithm of γ_{eq} is more consistent with the measured hysteresis loops.

TABLE 2 Parameters for the site response analysis of the Port Island borehole array site

	DCZ model								Excess pore water pressure model							
	A		B		γ_r ($\times 10^{-4}$)		λ_0 (%)						M		N	
Soil	H	H+V	H	H+V	H	H+V	H	H+V	C_1	C_2	C_3	γ_{th} ($\times 10^{-4}$)	H	H+V	H	H+V
Gravel 1	0.89	1.03	0.44	0.50	8.4	9.0	3.5	3.5	–	–	–	–	–	–	–	–
Gravel 2	0.89	1.03	0.44	0.50	8.7	9.0	3.5	3.5	1.193	0.134	1.25	2.0	0.43	0.45	25.34	24.46
Gravel 3	0.89	1.03	0.44	0.50	8.7	9.0	3.5	3.5	1.193	0.134	1.25	2.0	0.43	0.45	25.34	24.46
Gravel 4	0.89	1.07	0.44	0.52	9.5	10.7	3.5	3.5	1.193	0.134	1.25	2.0	0.43	0.45	25.34	24.46
Gravelly sand 1	1.03	1.08	0.51	0.52	9.7	11.1	3.2	3.2	0.733	0.191	1.17	2.0	0.48	0.48	16.58	16.58
Alluvial clay	1.28	1.19	0.60	0.60	13.6	13.2	3.2	3.2	–	–	–	–	–	–	–	–
Sand 1	1.07	1.06	0.50	0.50	15.6	17.6	3.2	3.2	0.654	0.214	1.07	2.0	0.45	0.44	15.55	16.55
Sand/gravelly sand	1.07	1.06	0.50	0.60	26.5	26.5	3.2	3.2	0.602	0.216	1.05	2.0	0.45	0.44	15.55	16.55
Sand 2	1.07	1.06	0.56	063	18.6	20.6	2.5	3.0	–	–	–	–	–	–	–	–
Stiff alluvial clay	1.30	1.27	0.63	0.63	22.0	22.0	2.5	3.0	–	–	–	–	–	–	–	–
Gravelly sand 2	1.07	1.06	0.59	0.63	25.0	25.0	2.5	3.0	–	–	–	–	–	–	–	–

Note: H = unidirectional (horizontal) shaking; H+V = bidirectional (horizontal and vertical) shaking.

In Figure 7, the cyclic stress-strain loops obtained at cycles 1, 5, 25, 60, and 100 in the cyclic triaxial test are shown. Figures 6(C) and 7 reveal how cyclic degradation process accompanied by EPWP generation in the saturated sand specimen occurs with the number of cycles. As shown in Figure 7, the proposed effective stress method can be successfully applied to simulate the undrained cyclic stress-strain responses of the saturated sand specimen within the entire loading cycles. The conspicuous implication is that the new algorithm of γ_{eq} can capture accurately strain reversal points for each half-cycle loading, and its implementation can more realistically mirror the progressive process of EPWP generation and stress-strain response of the saturated fine sand specimens than the conventional algorithm of γ_{eq} under uniform cyclic loadings.

In summary, the proposed effective stress method can excellently characterize the progressive development of undrained responses for the liquefiable sand over wide ranges of D_r during undrained cyclic loadings.

5.2 | Benchmarking case: liquefied site of Port Island borehole array

The benchmarking case history is the Port Island borehole array site during the 1995 Kobe Earthquake. The soil liquefaction appears to have taken place in the reclaimed deposits known as "Masado" soils down to about 18 m depth with abundant evidence. The depth of the groundwater table is 3.0 m. The soil profile, the S- and P-wave velocity profiles, soil densities, and the depths of strong-motion seismographs at the array site are presented in Figure 8.[20,26,27,30,58] Due to the lack of available laboratory data, the $G/G_{\max}$ and ξ curves evaluated from the literature data[30,42] and the Chen et al[7] EPWP model parameters are calibrated by the trial values in priori. This trial-and-error procedure is applied with an objective of matching the recorded strong motions with simulated ones. The calibrated $G/G_{\max}$ and ξ curves for simulating the unidirectional (horizontal) shaking and bidirectional (horizontal and vertical) shaking are presented in Figure 8. Accordingly, the parameters of the DCZ model and the Chen et al[7] EPWP model as well as ξ_0 values are listed in Table 2.

The North-South (NS) and Up-Down (UD) components of the borehole at 83 m depth recordings are employed as input motions at the horizontal and vertical directions, respectively. The corresponding horizontal and vertical components of the borehole array at 32, 16, and 0 m depth recordings are used as benchmark responses. In this article, site responses to horizontal and vertical input motions are assumed to be the propagation of the vertically incident shear (S) and compression (P) waves, respectively. For the cases of unidirectional and bidirectional shakings, using the proposed effective stress method, the simulated and recorded horizontal and vertical motion accelerograms and the 5% damped spectral acceleration curves at the borehole depths with the seismographs are shown in Figures 9 and 10, respectively.

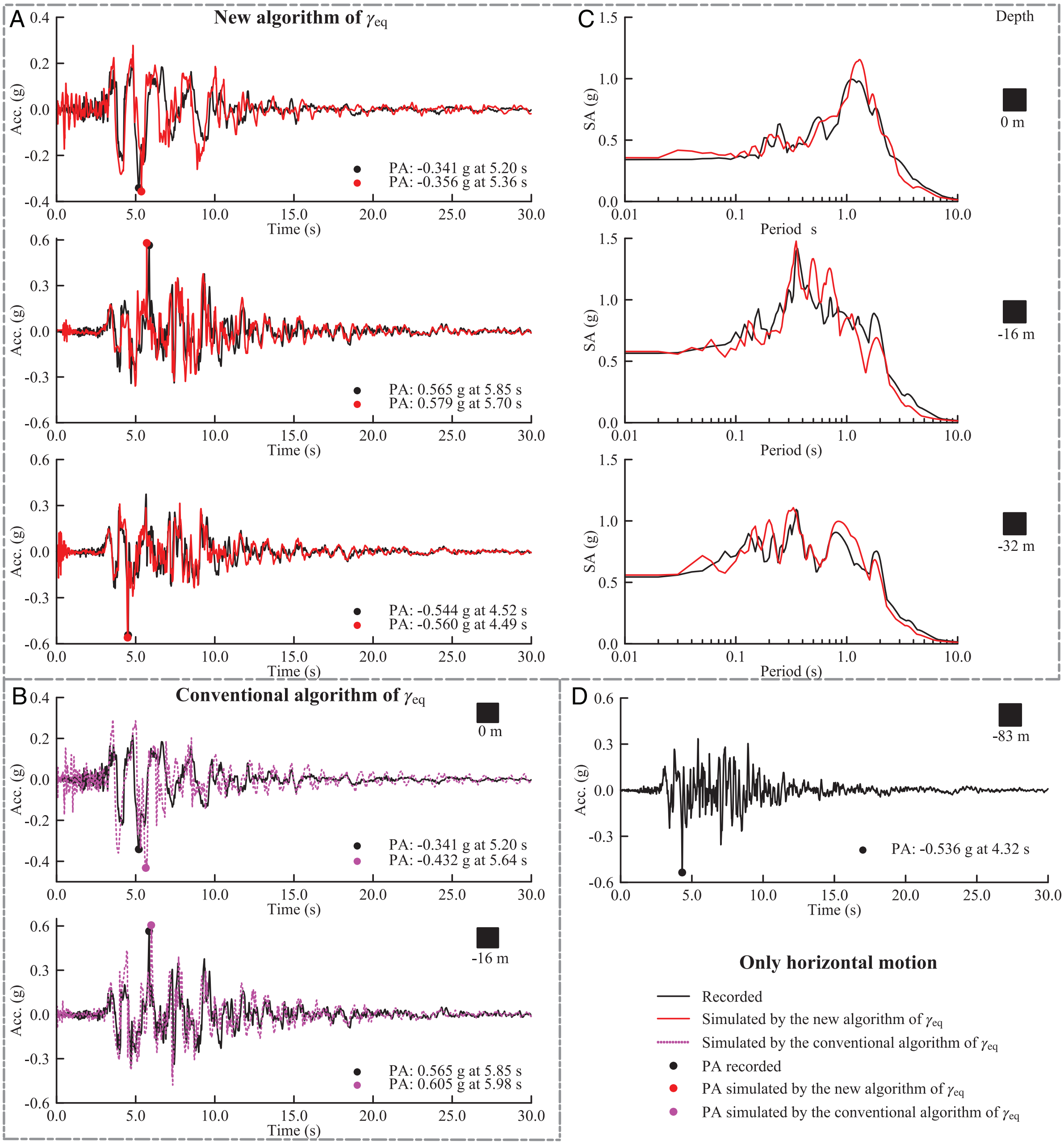

FIGURE 9 Comparisons of the simulated and recorded accelerograms and the corresponding spectral acceleration curves (5% damping) at the Port Island borehole array site for unidirectional (horizontal) shaking: (A) and (B) the acceleration time histories; (C) the spectral acceleration curves; and (D) input seismic motion. In this figure, g is gravitational acceleration; PA denotes peak acceleration. In the explicit dynamic analysis, time step: $\Delta t = 1 \times 10^{-5}$ seconds

Under either unidirectional or bidirectional shaking, the simulated horizontal or/and vertical motion accelerograms at various depths are generally quite consistent with the recordings. The peak accelerations and their locations at the time axis and the shapes of spectral acceleration curves recorded are well reproduced by the simulated results. The maximum disparity between the simulated and recorded peak accelerations at horizontal and vertical directions is less than 5% in all cases. The discrepancy between the simulated results and the records is considered acceptable, considering the epistemic uncertainties involved in the site model and the soil parameters.

In addition, a special phenomenon in Figures 9 and 10 can be observed from the array records at the surface that the vertical component is strongly amplified due to the not fully saturated soil layers close to the surface and the horizontal component is significantly reduced due to the shallow soil liquefaction. The excellent consistency between the simulated results and the records suggests that the proposed effective stress method can capture the observed P-wave amplification

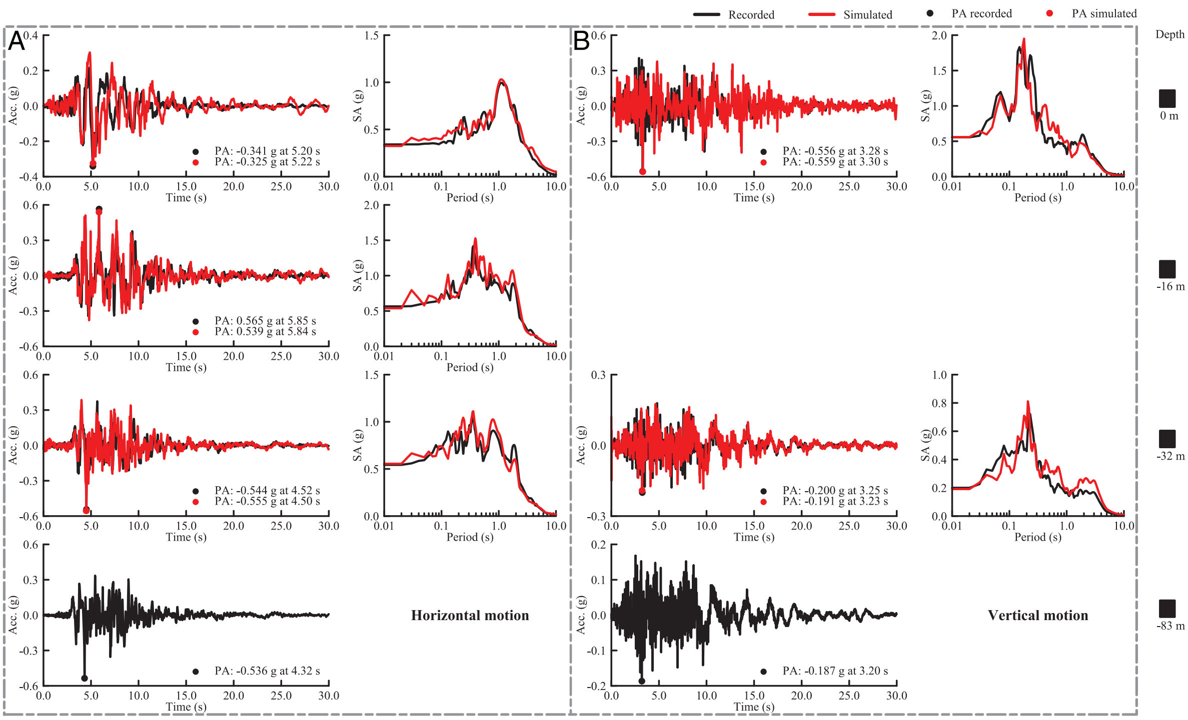

FIGURE 10 Comparisons of the simulated and recorded accelerograms and the corresponding spectral acceleration curves (5% damping) at the Port Island borehole array site for bidirectional (horizontal and vertical) shaking: (A) horizontal and (B) vertical. In this figure, g is gravitational acceleration; PA denotes peak acceleration. In the explicit dynamic analysis, time step: $\Delta t = 1 \times 10^{-5}$ seconds

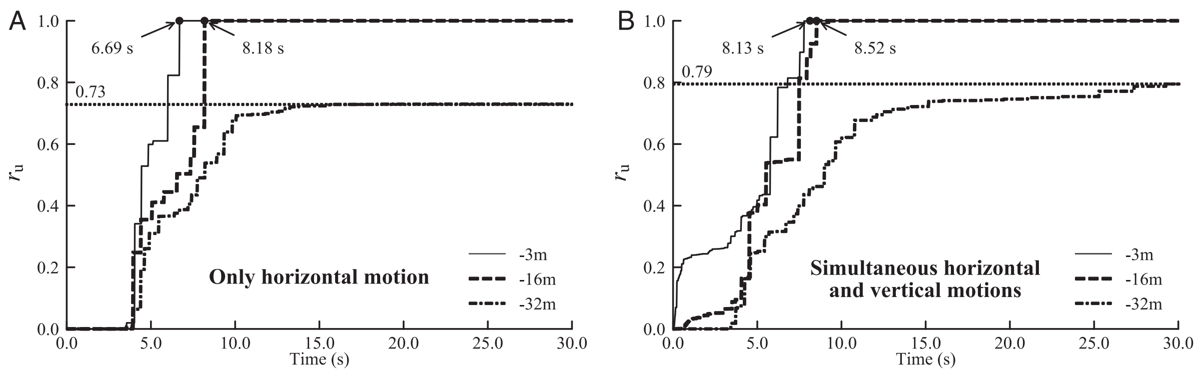

FIGURE 11 Simulated excess pore water pressure ratio r_u at the Port Island borehole array site: (A) unidirectional (horizontal) shaking and (B) bidirectional (horizontal and vertical) shaking

and S-wave attenuation. However, it is noted in Figure 9(B) that the simulated accelerograms using the the conventional algorithm of γ_{eq} are significantly inconsistent with the horizontal components of the borehole at 16 m and 0 m depth recordings, including the peak accelerations and their locations at the time axis. Besides, the moderate difference exists for calibrated the $G/G_{\max}$ and ξ curves as well as the ξ_0 through the inversion analyses of the unidirectional and bidirectional accelerograms of the borehole array. The important implication is that current understanding that the effect of vertical shaking on soil shear deformation behavior is negligible may not be always true, rather, the effect is dependent on the saturation condition of the soil and the coupling level of shear-compressional site response, as pointed out earlier by Yang.[56] It is also worth noting that the amplification of vertical motion at this borehole array site was significantly influenced by the saturation condition of near-surface fill.[57]

No data of EPWP at the borehole array site were recorded during the 1995 Kobe Earthquake. Figure 11 only depicts the generation of simulated r_u at the depths of 3, 16, and 32 m during the unidirectional and bidirectional shakings. The influence of vertical shaking on the generation of r_u is small for fully saturated soils. This result is consistent with the finding of Yang.[56] For the soils at the depths of 3 and 16 m, the r_u reached 100%, which resulted in full soil liquefaction. Meanwhile, the r_u of the sand layer at the depth of 32 m reached 73% and 79% for unidirectional and bidirectional shakings, respectively, which agree with the results of Cubrinovski and Ishihara[14] in which the range is between 60% and 85%.

In general, the new effective stress method for nonlinear site response analyses has the applicability to characterize the shear-compressional coupling response of deep soil profile with liquefiable layers over a wide strain range under unidirectional and bidirectional shakings. The simulation bias implies that there may be a limitation in the ideal soil column assumption and an uncertainty in the calibrated model parameters to characterize cyclic behavior of soils.

6 | CONCLUSIONS

This article presents a new algorithm for calculation of the equivalent shear strain (γ_{eq}) in 2D and 3D stress conditions in nonlinear dynamic analyses. This new algorithm of γ_{eq} is then integrated with the recently proposed 1D generalized non-Masing hysteresis model of Chen et al[6] (the DCZ model). The result is a new generalized non-Masing hysteresis model (the expanded DCZ model), which is simple and universal. The efficiency and accuracy of the new algorithm of γ_{eq} is demonstrated through a nonlinear response analysis of an element-level test subjected to tri-directional shakings. The proposed algorithm offers an attractive approach to improve the solution efficiency and accuracy in 2D and 3D large-scale nonlinear dynamic analyses.

Coupling the expanded DCZ model with the newly proposed excess pore water pressure generation model of Chen et al,[7] a new loosely coupled effective stress method for nonlinear site response analyses is proposed. This method allows a simulation of 1D, 2D, and 3D site responses of liquefaction susceptible soil deposits. The validation against the measured cyclic undrained responses of the benchmarking specimens demonstrates that the proposed method closely captures the features of the excess pore water pressure generation and the cyclic degradation behaviours of the axial stress-strain hysteresis loops.

The simulation results of the benchmarking liquefied site of the Port Island array validate the capability and applicability of the proposed effective stress method in capturing the important free-field response features of multilayered liquefiable sites: amplification and deamplification of seismic motions under unidirectional (horizontal) and bidirectional (horizontal and vertical) earthquake shakings. The simulations reproduce well the horizontal and vertical motion seismograms at different depths. The significant implication is that the new effective stress method permits the propagation of both high frequency and long period components of ground motions through liquefaction susceptible, multilayered soil deposits.

ACKNOWLEDGMENTS

This work was supported by the National Natural Science Foundation of China (51978334), the National Key R&D Project of China (2018YFC1504301, 2017YFC1500403), and the Research Grants Council of Hong Kong (17205717). This financial support is gratefully acknowledged.

ORCID

Guoxing Chen https://orcid.org/0000-0001-9185-7488

REFERENCES

1. Boulanger RW, Ziotopoulou K. *PM4Sand (Version 3.1): A Sand Plasticity Model for Earthquake Engineering Applications*. Davis, CA: Center for Geotechnical Modeling, Department of Civil and Environmental Engineering, University of California, USA; 2017. Report No. UCD/CGM-17/01.
2. Boulanger RW, Ziotopoulou K. *PM4Silt (Version 1): A Silt Plasticity Model for Earthquake Engineering Applications*. Davis, CA: Center for Geotechnical Modeling, Department of Civil and Environmental Engineering, University of California, USA; 2018. Report No. UCD/CGM-18/01.
3. Byrne PM. A cyclic shear-volume coupling and pore pressure model for sand. In Proceedings of 2nd International Conference on Recent Advances in Geotechnical Earthquake Engineering and Soil Dynamics, St. Louis, Missouri, USA, 1991: 47-55.
4. Chen GX, Chen L, Jing LP, Long H. Comparison of implicit and explicit finite element methods with parallel computing for seismic response analysis of metro underground structures. *J China Rail Soc*. 2011;33(11):112-117. in Chinese.
5. Chen GX, Jin DD, Zhu J, Shi J, Li XJ. Nonlinear analysis on seismic site response of Fuzhou Basin, China. *Bull Seismol Soc Am*. 2015;105(2a):928–949.
6. Chen GX, Ruan B, Zhao K, et al. Nonlinear response characteristics of undersea shield tunnel subjected to strong earthquake motions. *J Earthq Eng*. 2020;24(3):351–380.

7. Chen GX, Zhao DF, Chen WY, Juang CH. Excess pore pressure generation in cyclic undrained testing. *J Geotech Geoenviron Eng, ASCE*. 2019a;145(7):04019022.
8. Chen GX, Zhou ZL, Pan H, Sun T, Li XJ. The influence of undrained cyclic loading patterns and consolidation states on the deformation features of saturated fine sand over a wide strain range. *Eng Geol*. 2016;204:77-93.
9. Chen GX, Zhou ZL, Sun T, et al. Shear modulus and damping ratio of sand-gravel mixtures over a wide strain range. *J Earthq Eng*. 2019b;23(8):1407-1440.
10. Chiaradonna A, Tropeano G, d'Onofrio A, Silvestri F. Development of a simplified model for pore water pressure build-up induced by cyclic loading. *Bull Earthq Eng*. 2018;16(9):3627-3652.
11. Groholski DR, Hashash YMA, Kim B, Musgrove M, Harmon J, Stewart JP. Simplified model for small-strain nonlinearity and strength in 1D seismic site response analysis. *J Geotech Geoenviron Eng*. 2016;142(9):04016042. ASCE..
12. Cubrinovski M, Ishihara K. Modelling of sand behaviour based on state concept. *Soils Found*. 1998a;38(3):115-127.
13. Cubrinovski M, Ishihara K. State concept and modified elastoplasticity for sand modelling. *Soils Found*. 1998b;38(4):213-225.
14. Cubrinovski M, Ishihara K, Assessment of the Kobe Port Island liquefaction through analytical simulation of the vertical array records. In Proceedings of the Special Conference on Great Hanshin-Awafi Earthquake Disasters, Japan Society of Civil Engineers, January, Tokyo, 1996: 157-164.
15. Cubrinovski M, Rhodes A, Ntritsos N, Van Ballegooy S. System response of liquefiable deposits. *Soil Dynam Earthq Eng*. 2019;124:212-229.
16. Dobry R, Abdoun T. Recent findings on liquefaction triggering in clean and silty sands during earthquakes. *J Geotech Geoenviron Eng, ASCE*. 2017;143(10):04017077.
17. Dobry R, Pierce WG, Dyvik R, Thomas GE, Ladd RS. *Pore Pressure Model for Cyclic Straining of Sand*. Troy, New York: Research report, Rensselaer Polytechnic Institute; 1985.
18. DSSC. *Abaqus Analysis User's Manual, Version 6.14*. Providence, Rhode Island, USA: Dassault Systèmes Simulia Corp. (DSSC); 2014.
19. Finn WDL, Yogendrakumar M, Yoshida N, Yoshida H. *TARA-3: A Program to Compute the Response of 2-D Embankments and Soil-Structure Interaction Systems to Seismic Loadings*. Vancouver, BC: Department of Civil Engineering, University of British Columbia; 1986.
20. Foerster E, Modaressi H. Nonlinear numerical method for earthquake site response analysis II—case studies. *Bull Earthq Eng*. 2007;5(3):325-345.
21. Hashash YMA, Park D. Non-linear one-dimensional seismic ground motion propagation in the Mississippi embayment. *Eng Geol*. 2001;62(1):185-206.
22. Hashash YMA, Musgrove MI, Harmon JA, Groholski DR, Phillips CA, Park D. *DEEPSOIL 6.1, User Manual*. Urbana, Illinois: Board of Trustees of University of Illinois at Urbana-Champaign; 2016.
23. Huo H. *Seismic Design and Analysis of Rectangular Underground Structures*. West Lafayette, Indiana, USA: Purdue University; 2005.
24. ICC. *International Building Code*. Washington, DC: International Code Council (ICC); 2012.
25. Idriss IM, Boulanger RW. *Soil Liquefaction During Earthquakes. Monograph MNO-12*. Oakland, CA, USA: Earthquake Engineering Research Institute; 2008.
26. Ishihara K, Yasuda S, Nagase H. Soil characteristics and ground damage. *Soils Found*. 1996;36(Special):109-118.
27. Iwasaki Y, Tai M. Strong motion records at Kobe Port Island. *Soils Found*. 1996;36(Special):29-40.
28. Karimi Z, Dashti S. Numerical and centrifuge modeling of seismic soil–foundation–structure interaction on liquefiable ground. *J Geotech Geoenviron Eng, ASCE*. 2016;142(1):04015061.
29. Kellezi L. Local transmitting boundaries for transient elastic analysis. *Soil Dynam Earthq Eng*. 2000;19(7):533-547.
30. Kokusho T, Satoh K, Matsumoto M. Nonlinear dynamic response of soil ground during 1995 Hyogo-ken nanbu earthquake. *Tsuchi-tu-Kiso*. 1995;43(9):39-43. in Japanese.
31. Li FR, Chen GX. Nonlinear seismic response characteristics of CAP1400 nuclear island structure on soft rock sites. *Sci Technol Nucl Install*. 2020:8867026.
32. Liu JB, Li B. A unified viscous-spring artificial boundary for 3-D static and dynamic applications. *Sci China Ser E: Eng Mater Sci*. 2005;48(5):570-584.
33. Liu JB, Gu Y, Du YX. Consistent viscous-spring artificial boundaries and viscous-spring boundary elements. *Chin J Geotech Eng*. 2006;28(9):1070-1075. in Chinese.
34. Liu JB, Tan H, Bao X, Wang DY, Li ST. Seismic wave input method for three-dimensional soil-structure dynamic interaction analysis based on the substructure of artificial boundaries. *Earthq Eng Eng Vibr*. 2019;18(4):747-758.
35. Lu J, Peng J, Elgamal A, Yang Z, Law KH. Parallel finite element modeling of earthquake ground response and liquefaction. *Earthq Eng Eng Vibr*. 2004;3(1):23-37.
36. Markham CS, Bray JD, Macedo J, Luque R. Evaluating nonlinear effective stress site response analyses using records from the Canterbury earthquake sequence. *Soil Dynam Earthq Eng*. 2016;82:84-98.
37. Martin GR, Finn WDL, Seed HB. Fundamentals of liquefaction under cyclic loading. *J Geotech Eng Div*. 1975;101(GT5):423-438.
38. Matasovic N, Vucetic M. *Seismic Response of Composite Horizontally-Layered Soil Deposits*. Los Angeles, CA: Civil Engineering Department, University of California; 1993. UCLA Research Report No. ENG-93-182.
39. Matasovic N, Ordóñez GA. *D-MOD2000—A Computer Program for Seismic Site Response Analysis of Horizontally Layered Soil Deposits, Earthfill Dams, and Solid Waste Landfills*. Washington, USA: GeoMotions, LLC: Lacey; 2012.
40. Miao Y, Yao EL, Ruan B, Zhuang HY, Chen GX, Long XH. Improved Hilbert spectral representation method and its application to seismic analysis of shield tunnel subjected to spatially correlated ground motions. *Soil Dynam Earthq Eng*. 2018a;111:119-130.

41. Miao Y, Yao E, Ruan B, Zhuang HY. Seismic response of shield tunnel subjected to spatially varying earthquake ground motions. *Tunnel Undergr Space Technol*. 2018b;77:216-226.
42. Miwa S, Ikeda T. Shear modulus and strain of liquefied ground and their application to evaluation of the response of foundation structures. *Struct Eng/Earthq Eng*. 2006;23(1):167-179.
43. National Academies of Sciences Engineering and Medicine (NASEM). *State of the Art and Practice in the Assessment of Earthquake-Induced Soil Liquefaction and Its Consequences*. Washington, DC: National Academies Press; 2016.
44. Numanoglu OA, Musgrove M, Harmon JA, Hashash YMA. Generalized non-Masing hysteresis model for cyclic loading. *J Geotech Geoenviron Eng, ASCE*. 2017;144(1):06017015.
45. Olson SM, Mei X, Hashash YMA. Nonlinear site response analysis with pore-water pressure generation for liquefaction triggering evaluation. *J Geotech Geoenviron Eng*. 2020;146(2):04019128.
46. Park T, Park D, Ahn JK. Pore pressure model based on accumulated stress. *Bull Earthq Eng*. 2015;13(7):1913-1926.
47. Phillips C, Hashash YMA. Damping formulation for nonlinear 1D site response analyses. *Soil Dynam Earthq Eng*. 2009;29(7):1143-1158.
48. Régnier J, Bonilla LF, Bard PY, et al. PRENOLIN: international benchmark on 1D nonlinear site-response analysis–Validation phase exercise. *Bull Seismol Soc Am*. 2018;108(2):876-900.
49. Ruan B, Zhao K, Wang SY, Chen GX, Wang HY. Numerical modeling of seismic site effects in a shallow estuarine bay (Suai Bay, Shantou, China). *Eng Geol*. 2019;260:105233.
50. Seed HB, Martin PP, Lysmer J. *The Generation and Dissipation of Pore Water Pressures During Soil Liquefaction*. Berkeley, USA: University of California; 1975. Report No. UCB/EERC-75/26.
51. Tao Y, Rathje E. Insights into modeling small-strain site response derived from downhole array data. *J Geotech Geoenviron Eng, ASCE*. 2019;145(7):04019023.
52. Tropeano G, Chiaradonna A, d'Onofrio A, Silvestri F. A numerical model for non-linear coupled analysis of the seismic response of liquefiable soils. *Comput Geotech*. 2019;105:211-227.
53. Vucetic M. *Pore Pressure Buildup and Liquefaction of Level Sandy Sites During Earthquakes*. Troy, New York: Rensselaer Polytechnic Institute; 1986. PhD Thesis.
54. Vucetic M, Dobry R. *Pore Pressure Build-Up and Liquefaction at Level Sandy Sites During Earthquakes*. Troy, New York: Research report, Rensselaer Polytechnic Institute; 1986.
55. Xu CS, Song J, Du XL, Zhao M. A local artificial-boundary condition for simulating transient wave radiation in fluid-saturated porous media of infinite domains. *Int J Num Methods Eng*. 2017;112(6):529-552.
56. Yang J. Reappraisal of vertical motion effects on soil liquefaction. *Geotechnique*. 2004;54(10):671-676.
57. Yang J, Sato T. Interpretation of seismic vertical amplification observed at an array site. *Bull Seismol Soc Am*. 2000;90(2):275-285.
58. Yang J, Sato T, Li XS. Nonlinear site effects on strong ground motion at a reclaimed island. *Canad Geotech J*. 2000;37(1):26-39.
59. Yang Z, Lu J, Elgamal A. *OpenSees Soil Models and Solid-Fluid Fully Coupled Elements: User's Manual*. Department of Structural Engineering. San Diego: University of California; 2008.
60. Youd TL, Carter BL. Influence of soil softening and liquefaction on spectral acceleration. *J Geotech Geoenviron Eng*. 2005;131(7):811-825.
61. Zhang XL, Li XJ, Chen GX, Zhou ZH. An improved method of the calculation of equivalent nodal forces in viscous-elastic artificial boundary. *Chin J Theor Appl Mech*. 2016;48(5):1126-1135. in Chinese.

How to cite this article: Chen GX, Wang YZ, Zhao DF, Zhao K, Yang J. A new effective stress method for nonlinear site response analyses. *Earthquake Engng Struct Dyn*. 2021;50:1595–1611.
https://doi.org/10.1002/eqe.3384